

Spatial Perspective Transform Estimation from Fourier Spectrum Analysis of 2D Patterns in 3D Space

IAN J. MAQUIGNAZ,^{1,*}

Electrical and Computer Engineering, Queen's University, Kingston, Ontario, Canada, K7L 3N6

^{1,*} ian.maquignaz@queensu.ca

RCV Lab ¹ <https://rcvlab.engineering.queensu.ca/>

Ingenuity Labs ¹ <https://ingenuitylabs.queensu.ca/>

Abstract: A novel approach to 3D surface imaging is proposed, allowing for the continuous sampling of 3D surfaces to extract localized perspective transformation coefficients from Fourier spectrum analysis of projected patterns. The mathematical relationship for Spatial-Fourier Transformation Pairs is derived, defining the transformation of spatial transformed planar surfaces in the Discrete Fourier Transform spectrum. The mathematical relationship for the twelve degrees of freedom in perspective transformation is defined and validated, asserting congruity with independent and uniform transform pairs for spatial Euclidean, similarity, affine and perspective transformations. This work expands on previously derived affine Spatial-Fourier Transformation Pairs and characterizes its implications towards 3D surface imaging as a means of augmenting (X,Y,Z)-(R,G,B) point-clouds to include additional information from localized sampling of pattern transformations.

© 2022 Ian J. Maquignaz under the terms of the [Creative Commons Attribution-ShareAlike 4.0 International License](https://creativecommons.org/licenses/by-sa/4.0/).

1. Introduction

From optical communication to digital image processing, frequency domain transformations are a prominent tool used in optical signal analysis [1] [2, p.249-354]. In recent years, the research community has taken a growing interest in 3-dimensional (3D) surface imaging for different applications including range sensing, object/facial recognition, dynamic projection, 3D map building, and localization for autonomous vehicles. To make these applications possible, the analysis of structured light (SL) and coded structured light (CSL) for surface profilometry and 3D surface imaging have been proposed. As demonstrated by Salvi et al.'s [3] summary of works from 1982 to 2009 and Geng's [4] review of recent advances in surface imaging technology, this can be accomplished through a multitude of different approaches with a wide range of operating characteristics. For the purpose of this work, methods are categorized as either discrete or continuous active-correspondence, with sub-categorization as spatial, temporal, or spatio-temporal multiplexing.

Discrete spatially multiplexed methodologies are prominent in consumer products through active-correspondence products such as the Microsoft Kinect v1 [5] and the Intel RealSense [6]. These products use infrared (IR) laser sources projected through diffraction gratings to project spatial patterns onto a scene which are visually imperceptible to a human observer and therefore unimpeding of an observer's viewpoint. Higher precision discrete methodologies have been proposed through spatio-temporal multiplexing, including recent work by Cole et al. [7] which proposed modulating imperceptible grey code patterns by controlling a DLP projector's digital mirroring device (DMD). This approach extends on previously reported spatio-temporal multiplexing of grey-codes by Cotting and Fuchs [8]. Consumer examples of multi-pattern/multi-shot approaches are limited, likely indicative of the increased hardware costs associated with pattern modulation and/or the requirement for stationary subjects [9]. As described by Cole et al.,

a 2D-search requires $\log_2(M) + \log_2(N)$ grey-code patterns to produce a $M \times N$ depth-map, thus requiring the projection of 22 unique patterns on a stationary subject for a 1920×1080 depth-map.

Continuous patterns offer a higher tolerance for distortion and defocused optics which can be advantageous [10, 11]. The single phase shifting (SPS) methods by Srinivasana et al. [12] and Guan et al. [13] employ sinusoidal gratings or fringe patterns to sense depth through phase shifts. Multiple phase shifting (MPS) methods extend these approaches through works such as Gushov et al. [14], although these methods do not extend beyond the analysis of phase components for sinusoidal signals. The Fourier Transform becomes predominant with single coded frequency multiplexing (SCFM) approaches with the proposition of Fourier-Transform fringe-pattern analysis for topography and interferometry [15], and the definition of Fourier Transform profilometry (FTP) in 1983 by Takeda et al. [16]. These early works were followed by Su et al. [17] who proposed the usage of a Ronchi grating to create a quasi-sine optical field which could be analyzed in the Fourier domain without overlapping the zero component and other higher spectra. Later works include a single-shot 3D shape measurement methodology using Frequency-multiplex Fourier-transform profilometry by Takeda et al. [18].

A review of FTP methodologies presented by Su and Chen in 2001 [19], concluded that FTP methodologies offer great potential for further improvements, which was followed by a decade of Fourier contributions [20–26]. Among these works, Gong and Zhang proposed using sinusoidal fringe pattern for defocused binary patterns, achieving 480×480 depth-maps at 4,000 Hz with believed potential to achieve 12,500 Hz by either lowering the projector resolution, or replacing it with a mechanical grating [27]. The predominant approach to Fourier analysis surface imaging is through phase shifting patterns, though some have explored higher dimensionality in Fourier transformations. Lin and Su [28] proposed using a two-dimensional (2D) FTP to provide better separation of depth information from speckle-like structure and discontinuity noise in fringe patterns, and Hallerman and Shirley [29] proposed extracting height profiles from time-varying speckle-intensity patterns using a 3D Fast Fourier Transform, but examples of such endeavours are sparse. Within these works, the optical emitters and sensory hardware used to enable FTP methodologies varies, with approaches such as Gong and Zhang's using off-the-shelf consumer projectors [27], and others such as Hallerman and Shirley [29] and Dresel et al's [30] using laser sources.

Recent approaches have evolved beyond pure depth estimation and introduced a new interest in pursuing a richer understanding of the properties of sensed surfaces. This includes works such as Jiang et al. [31] who proposed a two projector and one camera configuration to produce 3D shape measurements with reduced shadow by estimating the surface normal to reduce directional bias. Continuing with this initiative, the proposed method introduces a novel approach to pattern generation, embedding correspondences in the Fourier spectrum to enable the augmentation of point cloud data to include pattern transformation coefficients. This expansion on the capacities of Fourier-based surface imaging is possible through the definition of a mathematical framework for mapping spatial perspective transformations to the discrete Fourier spectrum. This work contrasts in approach from phase-oriented Fourier analysis prominent in previous works, and as will be demonstrated, offers new potential for CSL surface imaging.

The organization of the remainder of this paper is as follows: Section 2 introduces the Discrete Fourier Transformation and Perspective Transform Theorem as a means of deriving the proposed mathematical relationship between the spatial and Fourier domains as Spatial-Fourier Transformation Pairs (SFTP). Section 3 presents experimental results from the simulated transformation of images, validating the equations derived in Section 2 by demonstrating congruence between the mathematical and simulated models. Section 4 extends on Section 2 to define special cases of SFTP for translations and shearing onto the Z-axis (warp). The paper concludes with a summary and discussion in Section 5.

2. Spatial-Fourier Transformation Pairs

The proposed method allows for correspondences to be embedded and analyzed in the Fourier spectrum using a novel derivation rooted in the theory of Fourier and geometric transformation. For completeness in the derivation of the proposed perspective theorem for SFTP, some background in Fourier and transform theory is provided.

2.1. The Fourier and Discrete Fourier Transform

The well known and centuries old Fourier Transform (FT; \mathcal{F}), as shown in its 3D form by Equation 2, samples an infinite 3D space $f(x, y, z)$ and produces the equivalent frequency domain representation $F(u, v, w)$. This is achieved by taking the input spatial signal and decomposing it into sine and cosine components such that the spatial signal can be represented exactly in the frequency domain as the sum of infinite sine and cosine functions. The inverse of the FT (\mathcal{F}^{-1}) shown in Equation 3, returns a frequency domain image to the spatial domain without loss.

$$F(u, v, w) = \mathcal{F}(f(x, y, z)) \Leftrightarrow f(x, y, z) = \mathcal{F}^{-1}(F(u, v, w)) \quad (1)$$

$$F(u, v, w) = \int_{-\infty}^{\infty} \int_{-\infty}^{\infty} \int_{-\infty}^{\infty} f(x, y, z) e^{-2\pi i (ux + vy + wz)} dx dy dz \quad (2)$$

$$f(x, y, z) = \int_{-\infty}^{\infty} \int_{-\infty}^{\infty} \int_{-\infty}^{\infty} F(u, v, w) e^{2\pi i (ux + vy + wz)} du dv dw \quad (3)$$

Representing a continuous spatial image exactly in the frequency domain is impractical as the number of frequencies required to fully decompose an image is unbounded. To overcome this challenge, the Discrete Fourier Transform (DFT) can be used to impose boundaries on a FT, such that a discrete spatial signal can be represented in the frequency domain as the sum of a finite number of sampled sine and cosine functions. This is illustrated in Equation 5, where the FT is bound by the number of sampled frequencies M in the x -axis, N in the y -axis, and D in the z -axis, for a total of $M \times N \times D$ sampled frequencies. For consistency, throughout this work M and N are set respectively to the number of columns and rows in an input image. As will be discussed in the following section, for the purpose of this work D is implicitly set to a value of 1 for 2D spatial input.

$$F(u, v, w) = \sum_{x=0}^{M-1} \sum_{y=0}^{N-1} \sum_{z=0}^{D-1} f(x, y, z) e^{-2\pi i \left(\frac{ux}{M} + \frac{vy}{N} + \frac{wz}{D} \right)} \quad (4)$$

$$f(x, y, z) = \frac{1}{MND} \sum_{u=0}^{M-1} \sum_{v=0}^{N-1} \sum_{w=0}^{D-1} F(u, v, w) e^{2\pi i \left(\frac{ux}{M} + \frac{vy}{N} + \frac{wz}{D} \right)} \quad (5)$$

Limited derivations of the relationship between spatial transformations and the FT spectrum appear in the first (1977) and second edition (1987) of *Digital Image Processing* by Gonzalez and Wintz [32, p.47-78] [33, p.72-100] and (1996) *Digital Image Processing* by Castleman [34, p.178-186]. The relationship between spatial affine transformations and the FT spectrum has been previously defined by Bracewell et al. in 1993 [35]. Bracewell included derivations of the theorem for Euclidean, similarity, and affine transforms in *Fourier Analysis and Imaging* [36, p.154-161]. Derivations for Euclidean and similarity transformations appear in the second edition of *Digital Image Processing* by Gonzalez and Woods [37, p.210], but are subsequently omitted from the third and fourth editions of the same text [2, 38]. In this work, the derivation extends Bracewell's approach and combines it with the observations and notational convention set forth by Brigham [39, p.35] [40, p.30-47].

2.2. 3D Perspective Transform of 2D Planes

As described by Hartley and Zisserman [41], spatial transformations follow a well established hierarchy of classes, i.e. isometry, similarity, affinity, and perspectivity transformations. Each subsequent class in the hierarchy relaxes invariant properties, inheriting and expanding the degrees of freedom (DoFs) of previous classes. For example, affine transformations preserve parallel lines and represent six DoFs in 2D space, whereas perspective transformations preserve only collinearity and represents eight DoFs in 2D space [41, p.16-22]. These DoFs increase with dimensionality increasing affine transformations to twelve DoF in 3D space and perspective transformations to fifteen DoFs [41, p.59]. Equation 6 defines the transformation of a 2D point P represented in homogeneous coordinates, using perspective transformation A to produce point P' . The use of homogeneous coordinates adds the third dimension z , which is subsequently removed from P' by perspective divide to produce P'' as shown in Equation 7.

$$\begin{bmatrix} x' \\ y' \\ z' \end{bmatrix} = P' = AP = \begin{bmatrix} \chi_x & \psi_{yx} & \tau_x \\ \psi_{xy} & \chi_y & \tau_y \\ \psi_{xz} & \psi_{yz} & \chi_z \end{bmatrix} \begin{bmatrix} x \\ y \\ z=1 \end{bmatrix} \quad (6)$$

$$P'' = P' / z' \quad (7)$$

The elements of matrix A have been denoted with symbolic terms for scaling (χ), shear (ψ) and translation (τ) transformation coefficients. The scaling and translation elements are denoted as χ_{axis} and τ_{axis} , where the subscript indicates the impacted axis. Shearing elements denote two axes in subscript, where χ_{ab} denotes the proportion of dimension a to be added to dimension b . If expressed in terms of a planar image $f(x, y, 1)$, Equations 6 and 7 can be rewritten as Equation 8, transforming $f(x, y, 1)$ to planar image $f(x', y', 1)$ which can be referred to independently as $g(x, y, 1)$.

$$g(x, y, 1) = f(x', y', 1) = f\left(\frac{\chi_x x + \psi_{yx} y + \tau_x}{\psi_{xz} x + \psi_{yz} y + \chi_z}, \frac{\psi_{xy} x + \chi_y y + \tau_y}{\psi_{xz} x + \psi_{yz} y + \chi_z}, 1\right) \quad (8)$$

To simplify the relationship between spatial translation and phase in Fourier space, the transformation is decomposed to isolate translation. This is achieved by redistributing Equation 6 to produce Equation 9, where the perspective transform has been decomposed into matrix B for shear, rotation and scaling, and a separate matrix C for translation. The inverse of Equation 9 is illustrated in Equation 10.

$$P' = BP + C = \begin{bmatrix} \chi_x & \psi_{yx} & 0 \\ \psi_{xy} & \chi_y & 0 \\ \psi_{xz} & \psi_{yz} & \chi_z \end{bmatrix} \begin{bmatrix} x \\ y \\ z=1 \end{bmatrix} + \begin{bmatrix} \tau_x \\ \tau_y \\ \tau_z=0 \end{bmatrix} \quad (9)$$

$$P = B^{-1}(P' - C) \quad (10)$$

2.3. Derivation of Spatial-Fourier Transformation Theorem

Following the precedent and convention set forth by Bracewell et al. [35] in deriving the *Affine Theorem*, the *Perspective Theorem* for SFTP is derived here by recognizing that if there exists a mapping between spatial image $f(x, y, z)$ and frequency domain representation $F(u, v, w)$, then given Equation 8 for a perspective transformation and Equation 4 for a DFT, a mapping from $f(x', y', z')$ to $F(u', v', w')$ must exist.

Theorem 1 (Perspective Transformation Theorem) *If $f(x, y, z)$ has 3D DFT $F(u, v, w)$, then $g(x, y, z) = f\left(\frac{\chi_x x + \psi_{yx} y + \tau_x}{\psi_{xz} x + \psi_{yz} y + \chi_z z}, \frac{\psi_{xy} x + \chi_y y + \tau_y}{\psi_{xz} x + \psi_{yz} y + \chi_z z}, 1\right)$ has 3D DFT $G(u, v, w)$, with $G(u, v, w) = EF(u, v, w)e^{2\pi i(EC)}$, and $E = \begin{bmatrix} \frac{u}{M} & \frac{v}{N} & \frac{w}{D} \end{bmatrix} B^{-1}$.*

Proof. To derive this result, the inner product of $[u \ v \ w]^T$ and $[x \ y \ z]^T$ is recognized in the phase exponent $-2\pi i(ux + vy + wz)$ of the 3D Fourier transform of Equation 4. This inner product can be defined by Equation 11 for a spatial point P_s in an $M \times N$ image with homogeneous 3rd dimension D .

$$\frac{ux}{M} + \frac{vy}{N} + \frac{wz}{D} = \begin{bmatrix} \frac{u}{M} & \frac{v}{N} & \frac{w}{D} \end{bmatrix} P_s \quad (11)$$

$$\frac{ux}{M} + \frac{vy}{N} + \frac{wz}{D} = \begin{bmatrix} \frac{u}{M} & \frac{v}{N} & \frac{w}{D} \end{bmatrix} B^{-1}(P'_s - C) \quad (12)$$

The perspective transformation coefficients can be substituted into Equation 11 to produce Equation 12. This substitution is possible by taking the inverse of the perspective transformation as shown in Equation 10.

$$\frac{ux}{M} + \frac{vy}{N} + \frac{wz}{D} = E(P'_s - C), \text{ where } E = \begin{bmatrix} \frac{u}{M} & \frac{v}{N} & \frac{w}{D} \end{bmatrix} B^{-1} \quad (13)$$

Reducing Equation 12 into Equation 13, components can then be re-substituted back into Equation 4 to produce Equation 14, mapping spatial image $f(x', y', z')$ to frequency representation $F(u', v', w')$.

$$F(u', v', w') = \sum_{x=0}^{M-1} \sum_{y=0}^{N-1} \sum_{z=0}^{D-1} f(x', y', z') e^{-2\pi i(E P'_s)} e^{2\pi i(EC)} \quad (14)$$

This completes the derivation of the theorem, proving the existence of a mapping for 2D spatial perspective transformations between frequency domain images $F(u, v, w)$ and $F(u', v', w')$.

Following the precedent of Equation 8, the spatial perspective transformation of a frequency domain image $F(u, v, w)$ to $F(u', v', w')$ can be expressed as Equation 16. This reduction is possible by substituting $F(u, v, w)$ for the Fourier Transform component expressed in Equation 4, re-writing periodicity terms in E as shown in Equation 15 (see Section 4.1) and retaining only spatial perspective transformation coefficients H and $e^{2\pi i(EC)}$, which respectively represent a transformation of frequency space and a phase-shifting component. To simplify, the mapping can be expressed as Equation 17, which provides the mapping in terms frequency points P_f and P'_f , as previously demonstrated for spatial points P_s and P'_s in Equation 6.

$$H = \begin{bmatrix} u & v & w \end{bmatrix} B^{-1} \quad (15)$$

$$F(u', v', w') = HF(u, v, w)e^{2\pi i(EC)} \quad (16)$$

$$P'_f = HP_f e^{2\pi i(EC)}, \text{ where } P_f = \begin{bmatrix} u & v & w \end{bmatrix}^T \quad (17)$$

2.4. Perspective Transformation Pairs

To increase understanding and utility of SFTP, short derivations of Equation 17 can be used as transformation pairs, defining mappings of Fourier space for simple spatial transformations. Such pairs are possible by recognizing the relationship between spatial and Fourier space as shown in Equation 1 and redefining in terms of pairwise relationships as shown in Equation 18.

$$f(x, y) \Leftrightarrow F(u, v) \quad (18)$$

$$|F(u, v)| = \sqrt{R(u, v)^2 + I(u, v)^2} \quad (19)$$

Taking the magnitude of the Fourier spectrum using Equation 19, the real and imaginary spectra of the Fourier transform are concatenated to produce a single representation invariant of spatial translation. This allows for the isolation of perspective transformation coefficients and the simplification of Equation 17 to Equation 20:

$$P'_F = HP_F \quad (20)$$

Using Equation 20, transform pairs can be derived for a subset of isometric, similarity, affine and perspective transformations. Table 1 summarizes a number of these derivations. Translation and shearing onto the Z-axis (warp) represent special cases and are described in Section 4.

Table 1. 2D Transformation pairs

<i>Rotation:</i>	$f(\cos(\theta)x + \sin(\theta)y, \cos(\theta)y - \sin(\theta)x, 1)$ $\Leftrightarrow F(\cos(\theta)u - \sin(\theta)v, \cos(\theta)v + \sin(\theta)u, 1)$
<i>Scaling:</i>	$f(\chi_x x, \chi_y y, 1) \Leftrightarrow F\left(\frac{u}{\chi_x}, \frac{v}{\chi_y}, 1\right)$ $f(\chi_x x, \chi_y y, \chi_z z) \Leftrightarrow F\left(\frac{u}{\chi_x}, \frac{v}{\chi_y}, \frac{w}{\chi_z}\right)$
<i>Shearing:</i>	$f(x + \psi_{yx}y, y + \psi_{xy}x, 1) \Leftrightarrow F\left(\frac{u - \psi_{xy}v}{1 - \psi_{yx}\psi_{xy}}, \frac{v - \psi_{yx}u}{1 - \psi_{yx}\psi_{xy}}, 1\right)$

3. Experimental Validation

To validate Theorem 1, a experiment was designed to emulate the operation of a Projector-Camera (PROCAM) pair in a real-world environment. In this configuration, the projection and subsequent imaging of 2D patterns in 3D space was emulated, providing validation of the derived SFTP and confirmation of its applicability towards the proposed application of surface sensing. To achieve this, images were encoded with known frequency domain patterns and subjected to known transformations in the spatial domain, allowing for empirical measurement of conformance between Equation 20 and transformations measured from imaging.

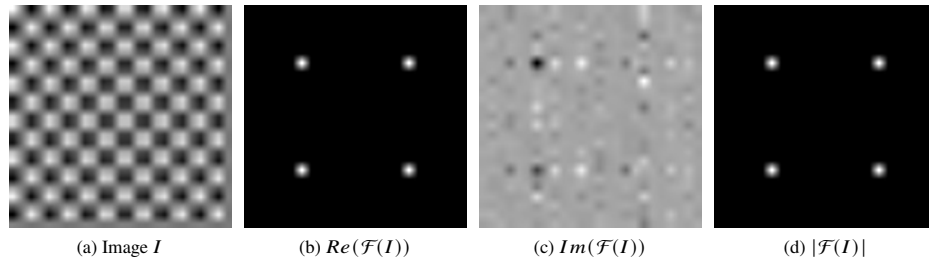


Fig. 1. A sample set of unaltered encoded images used for validation.

As a base, an image of size 25×25 was selected and encoded in the frequency domain with four frequencies of amplitude 10,000 at Cartesian coordinates (6, 6), (−6, −6), (6, −6), and (−6, 6) of the Fourier spectrum $F(u, v)$. To accommodate the use of Cartesian coordinates, the Fourier spectrum was reshaped to Cartesian representation using Equation 21, centering the

Fourier zero-frequency (ZF) to the Cartesian origin (0,0). This reshaping and its impact on the interpretation of the Fourier spectrum can be visualized through the transformation of Figure 2a to Figure 2b. The resulting spatial image and its Fourier decomposition are illustrated in Figure 1, with its spatial representation shown in Figure 1a, real component of the Fourier spectrum in Figure 1b, imaginary component in Figure 1c, and magnitude in Figure 1d. To allow visualization of the spatial and Fourier spectrums, spatial transformation employed bilinear interpolation and all images represented in this work are normalized by Equation 22 to redistribute image minimum f_{MIN} and maxima f_{MAX} of the spectrum values to a uniform range of $MIN = 0$ to $MAX = 255$. To increase understanding of the Fourier spectrum, images of the frequency domain have the ZF zeroed to facilitate normalization.

$$f(x, y)(-1)^{x+y} \Leftrightarrow F(u - \frac{M}{2}, v - \frac{N}{2}) \quad (21)$$

$$||f(x, y)|| = MIN + \frac{(f(x, y) - f_{MIN}) * (MAX - MIN)}{f_{MAX} - f_{MIN}} \quad (22)$$

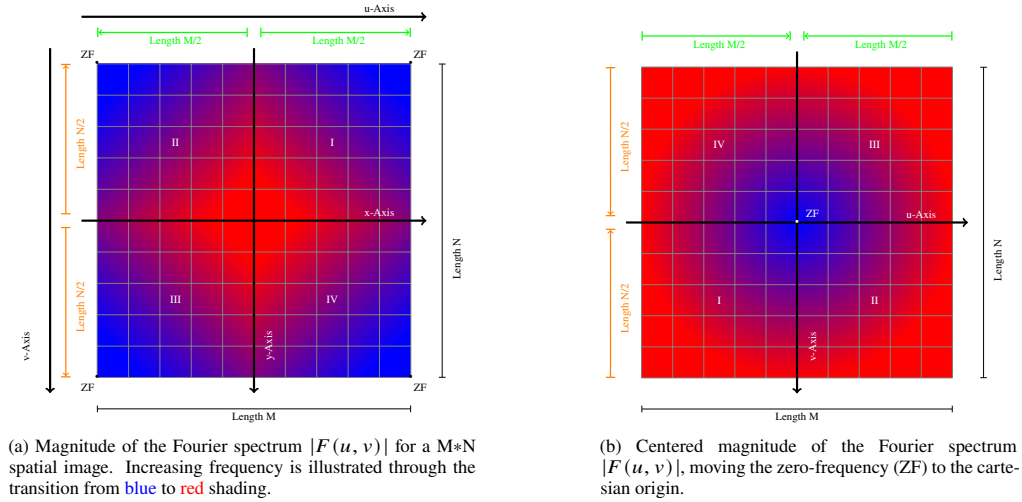


Fig. 2. The DFT spectrum (2a) and Centered DFT spectrum (2b)

Figure 3 illustrates five samples taken to validate independent and uniform scaling of the x , y and z -axes. To facilitate interpretation, Table 2 summarizes the estimated and captured coordinates for each of the images in Figure 3, with transformed coordinates identified as the four highest normalized cross-correlated template matched values in $|F(u, v)|$. This illustrates the conformity between the estimated and experimental results, with minor rounding resulting from integer pixel coordinates. This conformity is mirrored for shearing transformations as illustrated in Figure 4 and summarized in Table 3.

To demonstrate continuity in conformance, samples were collected for a granular range of coefficients, sampling independent and uniform rotation, scaling $\chi_x, \chi_y, \chi_z, \chi_x = \chi_y$, and $\chi_x = \chi_y = \chi_z$, and shearing ψ_{yx}, ψ_{xy} , and $\psi_{yx} = \psi_{xy}$. Using the experimental platform previously described, scaling coefficients were incremented by 0.005 between 0.75 and 1.25 for a total of 101 samples, shearing coefficients were incremented by 0.002 between 0.002 and 0.3 for a total of 150 samples, and rotation was sampled at 1 degree increments between 0 and 360 degrees. A subset of these tables are plotted in Figure 5, showing the congruence between captured and estimated points in $|F(u', v', z')|$ images for a range of transformation coefficients.

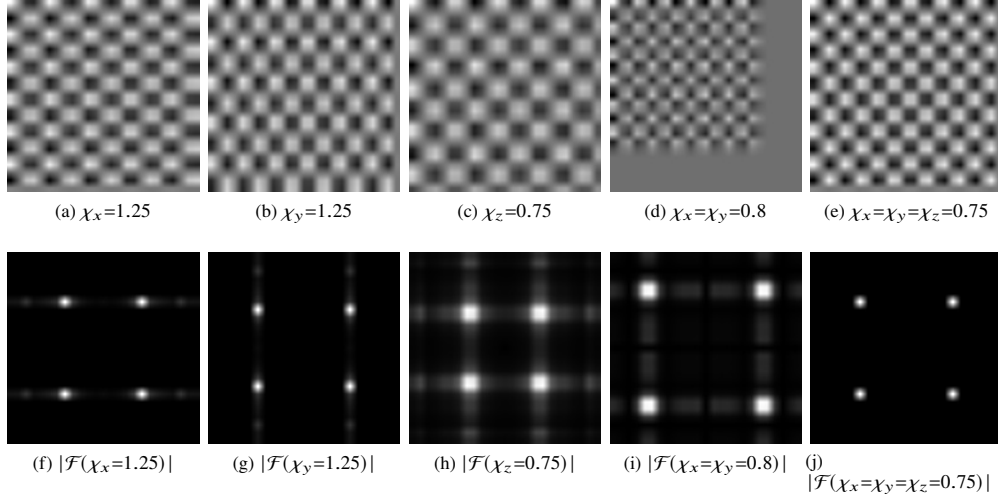


Fig. 3. Independent and uniform spatial scaling transformations of the x , y & z -axes

Table 2. Independent and uniform spatial scaling transformations of the x , y & z -axes

Transform	Captured Points	Calculated Points	Estimated Transform
$\chi_x = 1.25$	(5, 6)(-5, -6)(5, -6)(-5, 6)	(5, 6)(-5, -6)(5, -6)(-5, 6)	$\chi_x = 1.25$
$\chi_y = 1.25$	(6, 5)(-6, -5)(6, -5)(-6, 5)	(6, 5)(-6, -5)(6, -5)(-6, 5)	$\chi_y = 1.25$
$\chi_z = 0.75$	(5, 5)(-5, -5)(5, -5)(-5, 5)	(5, 5)(-5, -5)(5, -5)(-5, 5)	$\chi_z = 0.75$
$\chi_x = \chi_y = 0.8$	(7, 7)(-7, -7)(7, -7)(-7, 7)	(7.5, 7.5)(-7.5, -7.5)(7.5, -7.5)(-7.5, 7.5)	$\chi_x = \chi_y = 0.8$
$\chi_x = \chi_y = \chi_z = 0.75$	(6, 6)(-6, -6)(6, -6)(-6, 6)	(6, 6)(-6, -6)(6, -6)(-6, 6)	$\chi_x = \chi_y = \chi_z = 0.75$

Table 3. Independent and uniform spatial shearing and rotation transformations of the x & y -axes

Transform	Captured Points	Calculated Points	Estimated Transform
$\psi_{yx} = 0.3$	(6, 8)(-6, -8)(6, -4)(-6, 4)	(6, 7.8)(-6, -7.8)(6, -4.2)(-6, 4.2)	$\psi_{yx} = 0.3$
$\psi_{xy} = 0.3$	(8, 6)(-8, -6)(4, -6)(-4, 6)	(7.8, 6)(-7.8, -6)(4.2, -6)(-4.2, 6)	$\psi_{xy} = 0.3$
$\psi_{yx} = \psi_{xy} = 0.2$	(7, 7)(-7, -7)(5, -5)(-5, 5)	(7.5, 7.5)(-7.5, -7.5)(5, -5)(-5, 5)	$\psi_{yx} = \psi_{xy} = 0.2$
30° Rotation	(2, 8)(-2, -8)(8, -2)(-8, 2)	(2.196, 8.196)(-2.196, -8.196) (8.196, -2.196)(-8.196, 2.196)	30° Rotation
60° Rotation	(8, 2)(-8, -2)(2, -8)(-2, 8)	(8.196, 2.196)(-8.196, -2.196) (2.196, -8.196)(-2.196, 8.196)	60° Rotation

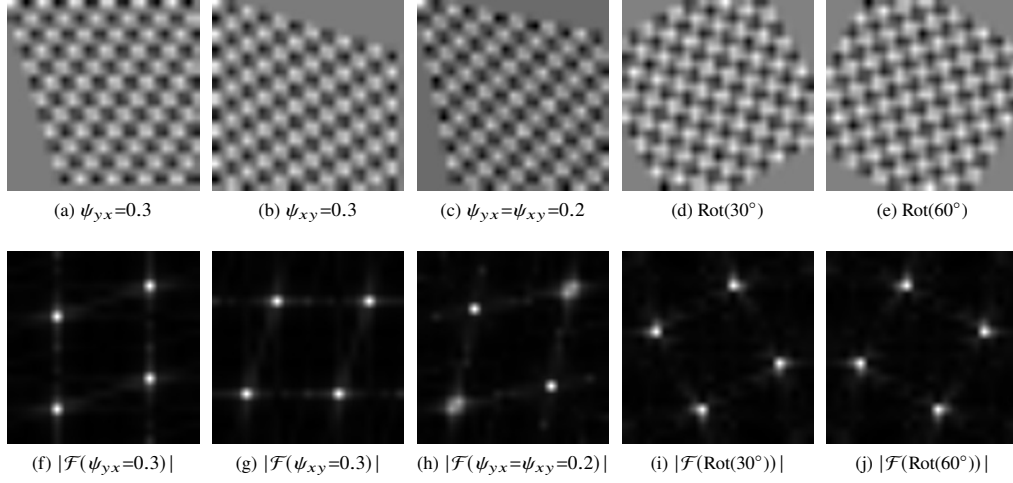


Fig. 4. Independent and uniform spatial shearing and rotation transformations of the x & y -axes

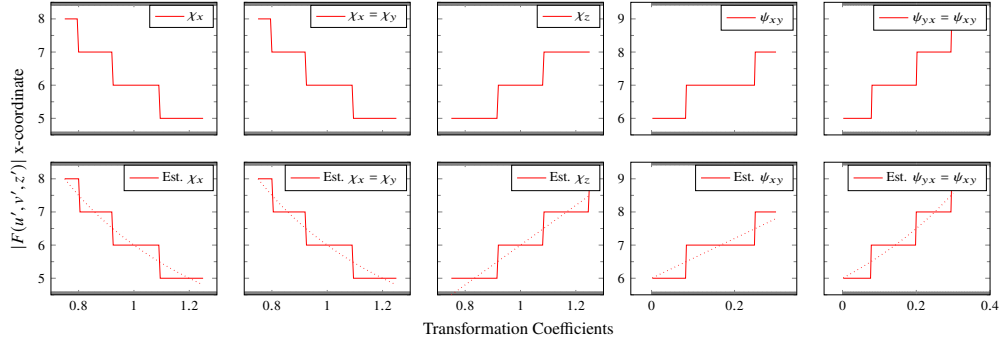


Fig. 5. Independent and uniform spatial scaling and shearing of the X , Y and Z axes. Top row plots illustrate experimentally captured results. Bottom row plots illustrate transformation estimations using Equation 17, with discrete integer estimation illustrated by a solid line and continuous floating-point estimation by a dotted line.

4. Special Cases

Special cases exist in Theorem 1 for SFTP which include spatial translations and transformations in higher dimensional space. Such spatial transformations alter the representation of the frequency domain, and visualization of the spectrum, as previous done using the magnitude of Equation 20, may not allow for a direct inference of the transformation. This section outlines transformation inference for these special cases, using Perspective Transform Theorem for SFTP as expressed in Equation 17.

4.1. Translation

Spatial translation does not manifest as a coordinate system transformation in the Fourier domain. Though expressed mathematically in Equation 17, spatial translation coefficients are omitted from the coordinate system transformation defined in Equation 20. This is a result of spatial translation representing a complex and spatially aware scaling of $F(u, v, w)$ which can be isolated and expressed through Equation 23:

$$G(u, v, w) = F(u, v, w)e^{2\pi i(E C)} \quad (23)$$

In DFTs, the impact of spatial transformations on the Fourier domain is proportional to the period of the sampled region. Defined by the relationships in Equation 24 and 25, translation along any dimension in multiples of the dimension's period will not result in alteration of the Fourier representation [37, p.210]. Translation in any dimension by increments other than the dimension's period will result in a quantifiable shift in the phase of Fourier domain frequencies.

$$f(x, y) = f(x + M, y) = f(x, y + N) = f(x + M, y + N) \quad (24)$$

$$F(u, v) = F(u + M, v) = F(u, v + N) = F(u + M, v + N) \quad (25)$$

To account for periodicity in DFTs, translation coefficients are scaled by the length of their respective dimensions M , N , and D as previously defined in Equation 4 and applied in E of Equation 23. This scaling is not applied to H in Equation 20 as the input points originate in Fourier space, and phase shifts are invariant in the magnitude of a DFT.

4.2. Validation of Translation

To validate Equation 23 for translation, 25×25 spatial samples were collected from 75×75 images which were encoded in the frequency domain. Applying Equation 25 for periodicity, encoding was implemented such that 25×25 samples of the image consisted of four frequencies with amplitude 10,000 at Cartesian coordinates $(6, 6)$, $(-6, -6)$, $(6, -6)$, and $(-6, 6)$ of the Fourier spectrum. This periodicity allowed for mitigation of noise from pattern truncation and for sampling of the central 25×25 region of the encoded image at one pixel increments from 0 to 25 pixels in the same manner as described in Section 3. Figure 6 illustrates a sample from this set.

The impact of Equation 23 on the Fourier spectrum can be measured by calculating the phase angles of each encoded point using Equation 26. To validate, Figure 7 illustrates the impact of spatial translation on the x -axis (τ_x) and uniformly on the x and y -axes ($\tau_x = \tau_y$) for one period of the encoded pattern. The magnitude of the spectrum remains constant throughout, and conformity between experimental and mathematically estimated results is illustrated respectively by Figures 7a and 7c and Figures 7b and 7d.

$$\Omega(u, v, w) = \arctan \left(\frac{I(u, v, w)}{R(u, v, w)} \right) \quad (26)$$

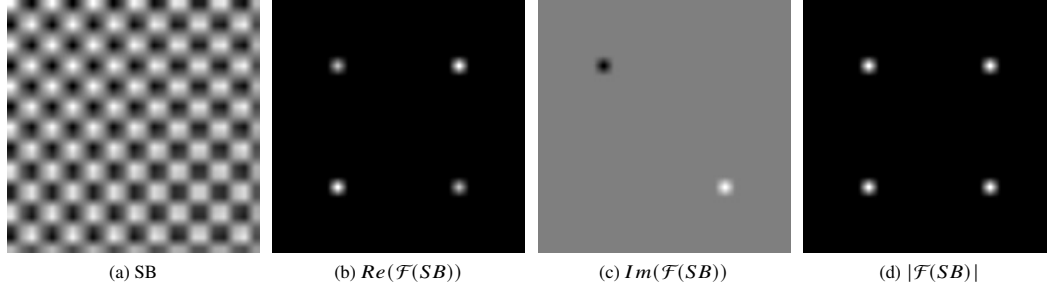


Fig. 6. Uniform spatial translation by six pixels $\tau_x = \tau_y = 6$

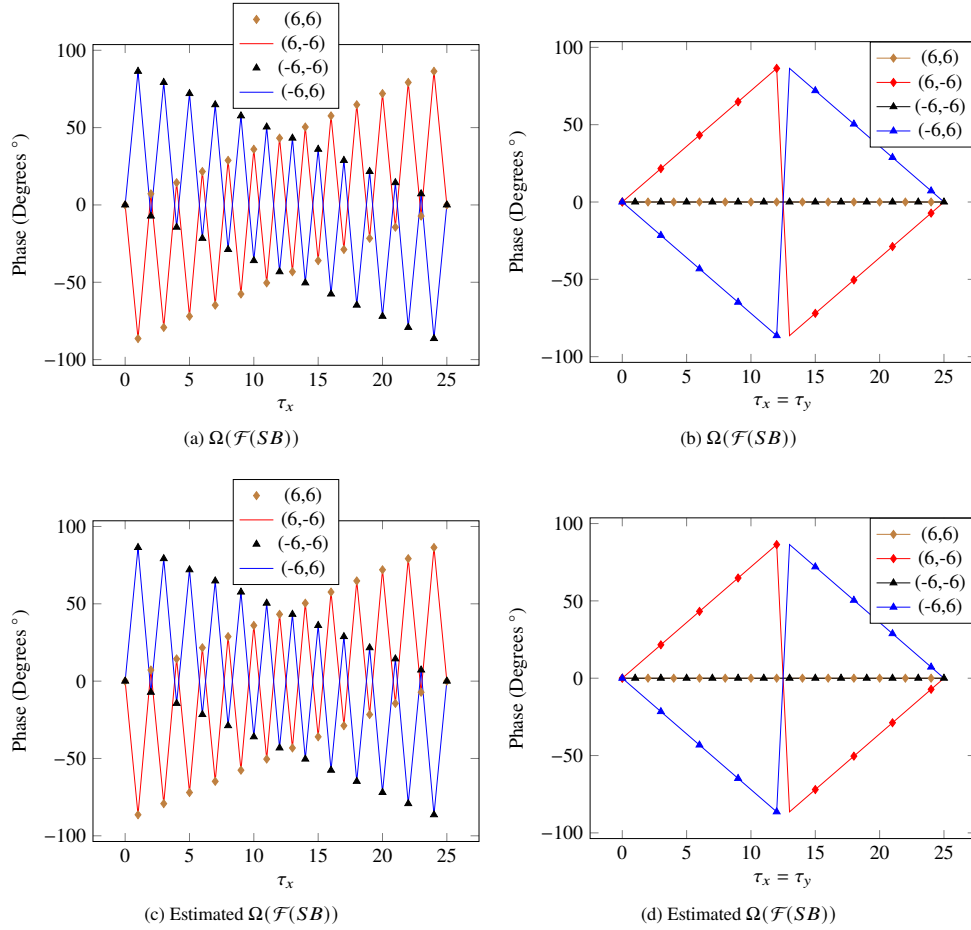


Fig. 7. Phase angles of encoded points from 25×25 samples translated by 0 to 25 pixels.

The Fourier spectrum has a $0.5 \times (M \times N)$ periodicity for $M \times N$ images and thus reflects across the zero frequency (Cartesian origin). Encoded points in the Cartesian quadrants I and III are the product of reflection and can be subject to destructive interference as seen in Figure 6c and the plots in Figure 7. Conformity between phase angles calculated through Equation 23 and experimental results in Figure 7 illustrate how translation is a measure of periodic misalignment

and further validates the Perspective Transformation Theorem for translation SFTP.

4.3. Shearing Onto the Z-axis

In 2D space, transformations such as a shearing of the x and y -axes onto the z -axis (warp, ψ_{xz} and ψ_{yz}) transform 2D input in 3D space. Often as an implicit step, a reduction in dimensionality is required to reduce the 3D result to the 2D dimensionality of the original input. The approach to validation used in this work simulates the projection and subsequent image capture of 2D patterns, allowing for projection in 3D space with implicit reduction to 2D space on re-capture. This implicit operation is synonymous with the application of Equation 7 after transformation, which can otherwise be restated for an image as Equation 27.

$$f\left(\frac{x'}{z'}, \frac{y'}{z'}, 1\right) = f\left(\frac{x'}{z'}, \frac{y'}{z'}, \frac{z'}{z'}\right) = f(x', y', z') \quad (27)$$

As a result, a 2D spatial image warped by $f(x, y, (\psi_{xz}x + \psi_{yz}y + z))$ is implicitly transformed by Equation 27 if 2D dimensionality is to be retained. This effectively alters the warp transformation to reflect a uniform scaling of the x and y -axes as shown in Equation 28. Inherent to this transformation, an interpolation algorithm is required to resolve the many-to-one pixel mappings from $f(x, y, z)$ to $f(x', y', z')$, for which many algorithms exist with varied pixel-binning characteristics.

$$f(x', y', 1) = f\left(\frac{x}{(\psi_{xz}x + \psi_{yz}y + z)}, \frac{y}{(\psi_{xz}x + \psi_{yz}y + z)}, \frac{(\psi_{xz}x + \psi_{yz}y + z)}{(\psi_{xz}x + \psi_{yz}y + z)}\right) \quad (28)$$

In the Fourier spectrum, this spatial transformation produces the complex conjugate shown in Equation 29 which preserves points $F(u, v, w)$ while introducing spatially-aware scaling as a factor of the x and y -axes. This phenomenon is illustrated in Figures 8 of a uniform spatial warp by 0.0075 ($\psi_{xz} = \psi_{yz} = 0.0075$). Figures 8f-8h illustrate the Fourier representation of the spatial image, including the smearing of encoded points towards higher frequencies in $F(u, v)$ space. This scaling is prominent in the II and IV Cartesian quadrants, though horizontal and vertical smearing can be seen in Figure 8h for all encoded points.

$$F(u', v', w') = JF(u, v, w) \quad (29)$$

$$\text{where } J = \begin{bmatrix} u & v & w \end{bmatrix} \begin{bmatrix} \frac{1}{(\psi_{xz}x + \psi_{yz}y + z)} & 0 & 0 \\ 0 & \frac{1}{(\psi_{xz}x + \psi_{yz}y + z)} & 0 \\ 0 & 0 & \frac{(\psi_{xz}x + \psi_{yz}y + z)}{(\psi_{xz}x + \psi_{yz}y + z)} \end{bmatrix}^{-1} \quad (30)$$

4.4. Validation of Warp

To validate SFTP perspective theorem for spatial warp transformations, 25×25 spatial images were encoded in the frequency domain with four frequencies of amplitude 10,000 at Cartesian coordinates $(6, 6)$, $(-6, -6)$, $(6, -6)$ and $(-6, 6)$ of the Fourier spectrum $F(u, v, w)$ as previously described in Section 3. Figure 8 illustrates a bilinearly interpolated and summing interpolation samples from this set, including the transformed spatial images in Figure 8a and 8e. The spatial representation shows the image deformation and the introduction of blank space (constant grey) to the right and bottom which will be represented as noise in frequency domain. This blank space cannot be mitigated through periodicity due to the spatially-aware nature of spatial warp transformations (see Equation 29).

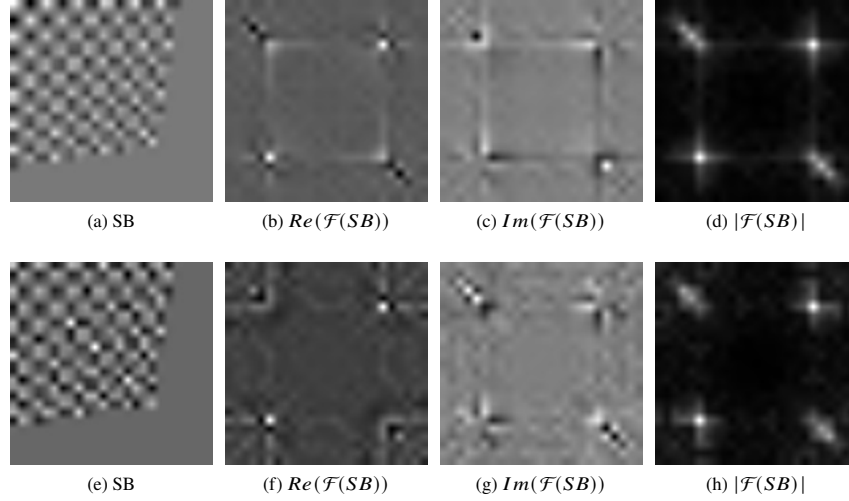


Fig. 8. A uniform spatial warp of the X & Y axes by 0.0075 ($\psi_{xz} = \psi_{yz} = 0.0075$). Figures 8a-8b use bilinear interpolation and Figures 8e-8f were interpolated using an arithmetic sum.

Table 4. Spatial shearing onto the Z-Axis (Warp)

Spatial Transform	$ \mathcal{F}(SB) $ Captured	$ \mathcal{F}(SB) $ Calculated	Estimated Transform
<i>None</i>	(6, 6)(-6, -6) (6, -6)(-6, 6)	(6, 6)(-6, -6) (6, -6)(-6, 6)	<i>None</i>
$\psi_{zx} = 0.003$	(6, 6)(-6, -6) (6, -6)(-6, 6)	(6.003, 6)(-5.997, -6) (6.003, -6)(-5.997, 6)	$\psi_{zx} = 0.003$
$\psi_{zy} = 0.003$	(6, 6)(-6, -6) (6, -6)(-6, 6)	(6, 5.997)(-6, -6.003) (6, -6.003)(-6, 5.997)	$\psi_{zy} = 0.003$
$\psi_{zx} = \psi_{zy} = 0.003$	(6, 6)(-6, -6) (7, -7)(-7, 7)	(6.003, 5.997)(-5.997, -6.003) (6.003, -6.003)(-5.997, 5.997)	$\psi_{zx} = \psi_{zy} = 0.003$

To validate uniform scaling of the frequency domain by spatial warp and ascertain conformity with Equation 29, sample images were transformed by spatial warp of the x -axis onto the z -axis (ψ_{xz}), y -axis onto the z -axis (ψ_{yz}) and the x & y -axes uniformly onto the z -axis ($\psi_{xz} = \psi_{yz}$). For each set, transformation coefficients were sampled at increments of 0.00005 over a range of 0.0 to 0.01 for a total of 201 samples per set. A select set of sampled transformations are shown in Table 4, showing estimation by Equation 29 for singular points. This table shows conformity with uniform scaling but poor handling of linearity due to estimation of singular points without spatial awareness, knowledge of neighboring pixels, or recursive transformation of the spatial range. This divergence between estimated and experimental results is pronounced for $\psi_{xz} = \psi_{yz}$ and occurs at later increments for ψ_{xz} and ψ_{yz} (not shown). The complete sampled range can be visualized in Figure 9 where to allow visualization of the non-uniform scaling shown in Equation 29 the solid lines represent values from the magnitude's maxima locations and the often overlapping dotted lines represent values from original encoded locations.

Vertices in the solid lines correspond to the changing of coordinates for the magnitude's maxima, where at the first vertex the solid curves diverge from the values of original encoded locations (dotted lines). Vertices occur at a warp of 0.0026 in Figure 9a and 0.002, 0.0037, 0.0042, and 0.006 in Figure 9e. From these plots, it can be observed that Cartesian quadrant pairs (quadrants mirrored in Fourier periodicity, I&III, and II&IV) often overlap and are impacted

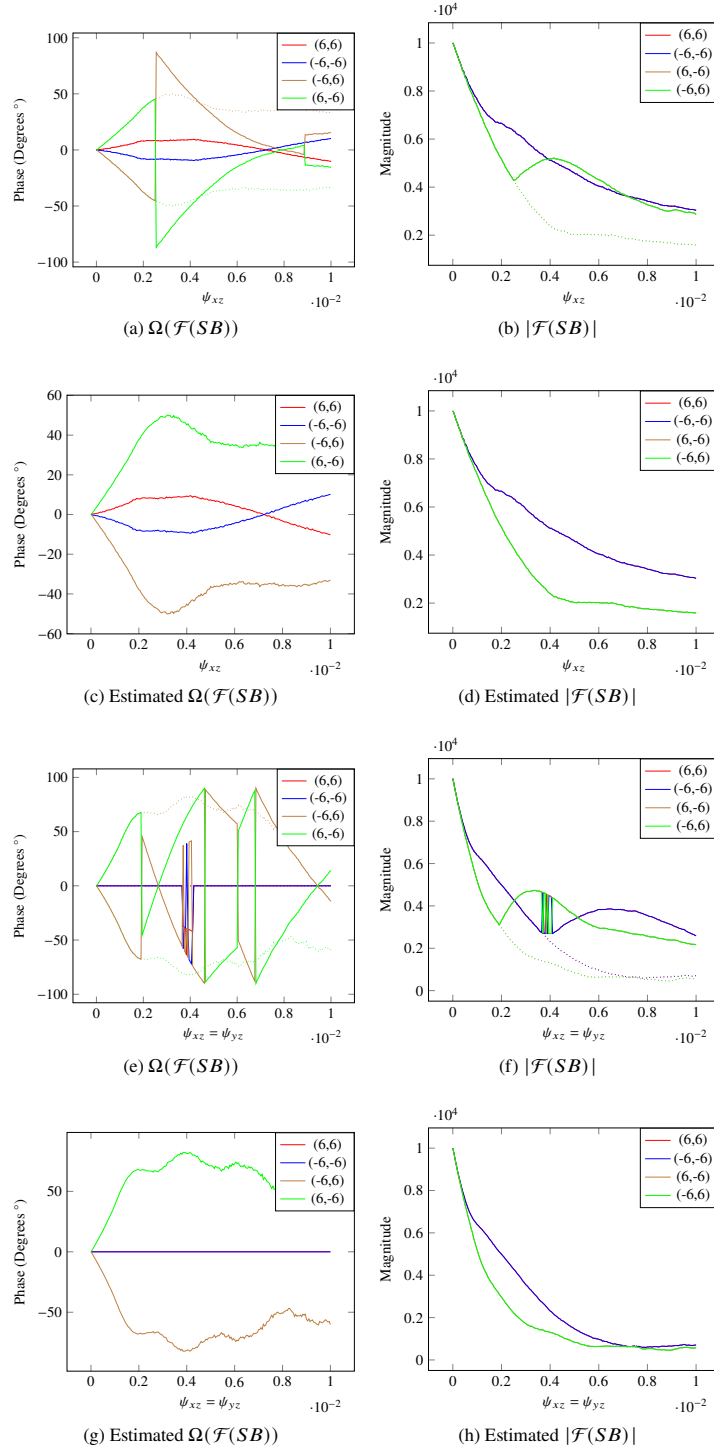


Fig. 9. Spatial shearing of the X and Y-axes onto the Z-axis (warp, ψ_{xz} and $\psi_{xz} = \psi_{yz}$) sampled at increments of 0.00005 from 0.0 to 0.01

uniformly. The values and corresponding figures for spatial warping of the y -axis have been omitted for they were visually identical to spatial warping of the x -axis illustrated in Figures 9a-9c.

5. Discussion

Bracewell et al.'s Affine Transformation Theorem created the foundation for the extension to perspective transformation pairs. For affine transformations, the novel formulation presented here reduces to Bracewell's equation, though it should be noted that equations reported are for DFT and more closely match the observations of *Fast Fourier Transform* and *Fast Fourier Transform And Its Applications* by Brigham [39, p.35] [40, p.30-47]. While this work has described these equations to model 2D images in 3D space, there is no theoretical limitation to extending the dimensionality of these equations. The selected scope was chosen to facilitate simulation and model real-world applications, although the mathematics of SFTP has been solved for spatial perspective transformations of 3D models in 3D space.

Through Section 3 and Section 4, it has been demonstrated that the Fourier spectrum can be sampled discretely and continuously. At lower levels of the transformation hierarchy this periodic property of DFTs allows for selective resolution in pattern sampling and thus control over the computational load. Though transformation coordinates in this work were sampled as the maxima of normalized cross-correlation template matching, future work can increase resolution and enable sub-pixel precision by modeling the decomposition of encoded values and increasing DFT frequency resolution.

$$C(u, v) = \alpha(u)\alpha(v) \cos\left(\frac{(2x+1)u\pi}{2 * N}\right) \cos\left(\frac{(2y+1)v\pi}{2N}\right) \quad (31)$$

$$\alpha(u) = \begin{cases} \sqrt{\frac{1}{N}} & \text{for } u = 0 \\ \sqrt{\frac{2}{N}} & \text{for } u = 1, 2, \dots, N-1 \end{cases} ; \alpha(v) = \begin{cases} \sqrt{\frac{1}{N}} & \text{for } v = 0 \\ \sqrt{\frac{2}{N}} & \text{for } v = 1, 2, \dots, N-1 \end{cases} \quad (32)$$

Future work includes potential pursuit of SFTP with other frequency domain algorithms such as Discrete Cosine Transform (DCT) to provide faster computational performance and more succinct results. As described by Gonzalez et al. [2, 475-478], there are few advantages and disadvantages to the implementation of a DCT over a DFT. Similar to DFTs, the computational time of a DCT is non-monotonic, so array sizes should be factor-able as a product of small prime numbers or padded for processing efficiency [42]. As documented by OpenCV [42] and described by Gonzalez et al. [2, p.477], 2D DCTs have a restriction to the resolution (periodicity) which forces the resolution of an $M \times N$ DCT to the size of one dimension. This is observable in Equation 31 where the periodicity of the u and v -axes of a DCT are set to $2N$.

DCTs are more computationally efficient than DFTs, largely as a result of being real-valued rather than complex-valued like DFTs. Though the frequency ranges expressed by DCTs and DFTs are almost the same, DCTs have double the frequency resolution of DFTs. This is a result of DFTs reflecting across the ZF, cutting the maximum number of frequencies in half. DCTs assume symmetry, meaning that the DCT of an N -point function $f(x)$ can be obtained from the DFT of a $2N$ -point symmetrically extended version of $f(x)$. This feature of DCTs minimizes boundary discontinuities which can introduce high-frequency components in DFTs. Overall, DCTs share many attributes with DFTs but set different assumptions and are more computationally efficient.

With respect to applications of this work, it is recognized that for any given encoded pattern, projected onto a flat incident surface, the DFT of the pattern can be utilized to interpret the uniform transformation of the encoded pattern from projector space to camera space. This is feasible as the transformation is uniform across the entirety of the captured image which provides a distinct Euclidean, similarity, affine or perspective transformation. For non-planar surfaces, the transformation of any point can be described on the tangent plane as a linear transformation by a

localized DFT. Using these principles, future work will explore the potential for spatio-temporal Fourier surface imaging sensors to recover surface normals.

6. Conclusions

In this work the mathematical relationship for Spatial-Fourier Transformation Pairs (SFTP) was derived, defining the transformation of spatial transformed planar surfaces in the Discrete Fourier Transform (DFT) spectrum. The mathematical relationship for the twelve degrees of freedom in perspective transformation was defined, expanding on previously derived affine Spatial-Fourier Transformation Pairs (SFTP). The Perspective Transformation Theorem was proposed as an extension to Bracewell et al.'s Affine Transformation Theorem. The theorem was validated experimentally, by transforming sample images in the spatial domain and analyzing them in Fourier space to assert congruity with independent and uniform transform pairs for Euclidean, similarity, affine and ultimately perspective transformations.

Funding

Epson Canada, Limited; Ontario Centers of Excellence (VIP II 27531); Natural Sciences and Engineering Research Council of Canada (NSERC) (CRDPJ506235-16).

Acknowledgments

The authors would like to acknowledge Epson Canada, the Natural Sciences and Engineering Research Council of Canada, and the Ontario Centres of Excellence, for their support of this work.

Disclosures

The authors declare no conflicts of interest.

References

1. K. Kikuchi, "Fundamentals of coherent optical fiber communications," *J. Light. Technol.* **34**, 157–179 (2016).
2. R. C. Gonzalez and R. E. Woods, *Digital Image Processing 4th Edition* (Pearson, 2018).
3. J. Salvi, S. Fernandez, T. Pribanic, and X. Llado, "A state of the art in structured light patterns for surface profilometry," *Pattern Recognit.* **43**, 2666 – 2680 (2010).
4. J. Geng, "Structured-light 3d surface imaging: a tutorial," *Adv. Opt. Photon.* **3**, 128–160 (2011).
5. Z. Zhang, "Microsoft kinect sensor and its effect," *IEEE MultiMedia* **19**, 4–10 (2012).
6. Intel Corporation, "Intel®realsensetmd400series product family," Accessed 14/2/2020.
7. A. Cole, S. Ziauddin, and M. Greenspan, "High-speed imperceptible structured light depth mapping," *Int. Conf. on Comput. Vis. Theory Appl.* (2020).
8. D. Cotting, M. Naef, M. Gross, and H. Fuchs, "Embedding imperceptible patterns into projected images for simultaneous acquisition and display," in *Third IEEE and ACM International Symposium on Mixed and Augmented Reality*, (2004), pp. 100–109.
9. Zivid, "Zivid," Accessed 17/1/2020.
10. M. J. Amin and N. A. Riza, "Active depth from defocus system using coherent illumination and a no moving parts camera," *Opt. Commun.* **359**, 135–145 (2016).
11. S.-Y. Chan, H.-F. Shih, and J.-S. Chen, "Depth measurement using structured light and spatial frequency," *Appl. Opt.* **55**, 5069–5075 (2016).
12. V. Srinivasan, H. C. Liu, and M. Halioua, "Automated phase-measuring profilometry: a phase mapping approach," *Appl. Opt.* **24**, 185–188 (1985).
13. C. Guan, L. G. Hassebrook, and D. L. Lau, "Composite structured light pattern for three-dimensional video," *Opt. Express* **11**, 406–417 (2003).
14. V. Gushov and Y. Solodkin, "Automatic processing of fringe patterns in integer interferometers," *Opt. Lasers Eng.* **14**, 311 – 324 (1991).
15. M. Takeda, H. Ina, and S. Kobayashi, "Fourier-transform method of fringe-pattern analysis for computer-based topography and interferometry," *J. Opt. Soc. Am.* **72**, 156–160 (1982).
16. M. Takeda and K. Mutoh, "Fourier transform profilometry for the automatic measurement of 3-d object shapes," *Appl. Opt.* **22**, 3977–3982 (1983).

17. L. G. Jian Li, Xianyu Su, "Improved fourier transform profilometry for the automatic measurement of three-dimensional object shapes," *Opt. Eng.* **29**, 1439 – 1444 – 6 (1990).
18. M. Takeda, Q. Gu, M. Kinoshita, H. Takai, and Y. Takahashi, "Frequency-multiplex fourier-transform profilometry: a single-shot three-dimensional shape measurement of objects with large height discontinuities and/or surface isolations," *Appl. Opt.* **36**, 5347–5354 (1997).
19. X. Su and W. Chen, "Fourier transform profilometry:: a review," *Opt. Lasers Eng.* **35**, 263 – 284 (2001).
20. W. Chen, X. Su, Y. Cao, Q. Zhang, and L. Xiang, "Method for eliminating zero spectrum in fourier transform profilometry," *Opt. Lasers Eng.* **43**, 1267 – 1276 (2005).
21. H.-M. Yue, X.-Y. Su, and Y.-Z. Liu, "Fourier transform profilometry based on composite structured light pattern," *Opt. & Laser Technol.* **39**, 1170 – 1175 (2007).
22. M. A. Gdeisat, D. R. Burton, and M. J. Lalor, "Eliminating the zero spectrum in fourier transform profilometry using a two-dimensional continuous wavelet transform," *Opt. Commun.* **266**, 482 – 489 (2006).
23. L.-s. Wu and Q.-j. Peng, "Research and development of fringe projection-based methods in 3d shape reconstruction," *J. Zhejiang Univ. A* **7**, 1026–1036 (2006).
24. W. Chen, P. Bu, S. Zheng, and X. Su, "Study on fourier transforms profilometry based on bi-color projecting," *Opt. & Laser Technol.* **39**, 821 – 827 (2007).
25. F. Berryman, P. Pynsent, J. Fairbank, and S. Disney, "A new system for measuring three-dimensional back shape in scoliosis," *Eur. Spine J.* **17**, 663–672 (2008).
26. E. Hu and Y. He, "Surface profile measurement of moving objects by using an improved π phase-shifting fourier transform profilometry," *Opt. Lasers Eng.* **47**, 57 – 61 (2009).
27. Y. Gong and S. Zhang, "Ultrafast 3-d shape measurement with an off-the-shelf dlp projector," *Opt. Express* **18**, 19743–19754 (2010).
28. X. S. Jin-Feng Lin, "Two-dimensional fourier transform profilometry for the automatic measurement of three-dimensional object shapes," *Opt. Eng.* **34**, 3297 – 3302 – 6 (1995).
29. G. R. Hallerman and L. G. Shirley, "Comparison of surface contour measurements based on speckle pattern sampling and coordinate measuring machines," in *Three-Dimensional Imaging and Laser-Based Systems for Metrology and Inspection II*, vol. 2909 (International Society for Optics and Photonics, 1997), pp. 89–97.
30. T. Dresel, G. Häusler, and H. Venzke, "Three-dimensional sensing of rough surfaces by coherence radar," *Appl. Opt.* **31**, 919–925 (1992).
31. C. Jiang, B. Lim, and S. Zhang, "Three-dimensional shape measurement using a structured light system with dual projectors," *Appl. Opt.* **57**, 3983–3990 (2018).
32. R. C. Gonzalez and P. A. Wintz, *Digital Image Processing* (Addison-Wesley, 1977).
33. R. C. Gonzalez and P. A. Wintz, *Digital Image Processing 2nd Edition* (Addison-Wesley, 1987).
34. K. R. Castleman, *Digital Image Processing* (Prentice-Hall, 1996).
35. R. N. Bracewell, K. . Chang, A. K. Jha, and Y. . Wang, "Affine theorem for two-dimensional fourier transform," *Electron. Lett.* **29**, 304– (1993).
36. R. Bracewell, *Fourier Analysis and Imaging* (Kluwer Academic/Plenum Publishers, 2003).
37. R. C. Gonzalez and R. E. Woods, *Digital Image Processing 2nd Edition* (Prentice-Hall, 2002).
38. R. C. Gonzalez and R. E. Woods, *Digital Image Processing 3rd Edition* (Pearson, 2011).
39. E. O. Brigham, *The Fast Fourier Transform* (Prentice-Hall, 1974).
40. E. O. Brigham, *The Fast Fourier Transform and Its Applications* (Prentice-Hall, 1988).
41. R. Hartley and A. Zisserman, *Multiple view geometry in computer vision* (Cambridge university press, 2003).
42. OpenCV, "Open source computer vision," <https://docs.opencv.org/4.1.0/index.html> (2019).